INTERNATIONAL JOURNAL FOR NUMERICAL METHODS IN FLUIDS, VOL. 14, 299–325 (1992)

COMPRESSIBLE GAS FLOW BETWEEN CLOSELY SPACED PLATES

ZISSIMOS P. MOURELATOS

Engine Research Department, General Motors Research Laboratories, Warren, Michigan 48090, USA.

SUMMARY

A theoretical analysis is presented to solve numerically the steady state Navier–Stokes equations, continuity equation and energy equation for a compressible ideal gas flow between two closely spaced, in general non-parallel, infinitely wide plates (slider bearing). The analysis includes the gas inertia effect and covers both non-choked and choked flows. The results of the present analysis compare very well with both analytical and experimental results of compressible flow in a slider bearing comprised of two parallel and stationary plates. It was found that for choked flow the gas inertia effect is important, while the consideration of the energy equation does not affect the accuracy of the calculated flow substantially. Finally, the stiffness of a slider bearing is presented for different geometrical characteristics of the bearing.

KEY WORDS Compressible gas bearing Choked flow Finite element method

INTRODUCTION

The need for an accurate analysis of compressible gas flow between closely spaced surfaces has arisen in connection with studies of externally pressurized bearings and leakage rates associated with gas seals. The gas inertia effect is important in such studies for an accurate flow calculation at the entrance and exit of the flow path.

A survey of the literature shows that considerable work related to the effect of fluid inertia in hydrodynamic lubrication has been done for both the laminar and turbulent flow cases. A large number of analyses have been made for incompressible fluids. For small inertia effect the method of averaged inertia has been used extensively.[3–6] It replaces the actual inertia terms by their average values in the equations of motion, leading to a Reynolds-type partial differential equation in pressure. However, the most serious assumption of the method is that the shape of the velocity is not influenced by inertia.

Kuzma[7] used a simple iteration scheme to account for the inertia effects in squeeze films. Small-perturbation analysis has also been used widely. The modified Reynolds number, or any other small parameter, can be used as the perturbation parameter for the expansion of velocities and pressure.[8–12] The perturation solution is valid for Reynolds numbers (Re) much less than one. For arbitrary Re, Tichy[13] developed a solution based on 'slug flow linearization' of the convective inertia terms, i.e. an Oseen-type approximation.

The qualitative difference in performance between incompressible liquids and gases generally vanishes as the Mach number approaches zero. However, in many gas bearing applications, such

* Author to whom correspondence should be addressed.

0271–2091/92/030299–27$13.50

Received 24 October 1989
Revised 2 April 1991

as externally pressurized gas bearings, the gas is considered compressible since the Mach number can reach large values. The density in the equations of motion and continuity is variable and depends on both pressure and temperature according to the equation of state. The gas viscosity is also dependent on both temperature and pressure. Therefore the temperature is also a variable in gas bearing analysis, in addition to the velocity components and the pressure. This requires the energy equation for the gas to be solved along with the Navier–Stokes equations (equations of motion), continuity equation and equation of state. Incorporation of the energy equation into the gas film analysis resolves the question of whether the gas expands isothermally or isentropically in the lubrication process.

Generally, when the flow Mach number is low, the inertia effects are small and a parabolic velocity profile across the film thickness is a reasonable assumption. However, if the Mach number is not low, the parabolic velocity profile may lead to incorrect results. In the literature, numerous gas flow analyses are based arbitrarily on the parabolic velocity profile assumption because it simplifies the calculations significantly.[1] A more exact analysis of inertia effects in longitudinal gas flow between parallel plates with no relative motion was performed by Elrod and Chu.[14] The energy equation was solved in conjunction with the two-dimensional boundary layer equations. The pressure was assumed to be constant across the film thickness. The equations were solved numerically for various entrance Mach numbers, assuming a uniform entrance velocity profile. The important result obtained was that for low Mach numbers the lubricating gas flow is isothermal, while for non-negligible Mach numbers the flow is approximately adiabatic but not isentropic. To our knowledge, the analysis performed by Elrod and Chu is the most realistic and relatively 'exact' analysis available in the literature for longitudinal gas flow.

In this paper an analysis is presented to solve numerically the steady state Navier–Stokes equations, continuity equation and energy equation for a compressible ideal gas in a two-dimensional space. The same analysis can be easily extended to the time-dependent case. The convective terms in the Navier–Stokes equations are retained, including the important inertia effect for high-velocity gas flow. The flow between two, in general non-parallel, surfaces is studied. One of the surfaces may also move relatively to the other surface. A pressure gradient is applied between the entrance and exit of the flow. This pressure gradient can be very large (approximately 13 800 kPa or 2000 lbf in^{-2}), simulating the pressure difference between the combustion chamber and the ambient close to TDC (top dead centre). Thus a combination of Couette and Poiseuille flow is considered. The analysis covers both non-choked and choked flows where the velocity at the exit is less than or equal to the local sonic velocity respectively. The viscosity of the working fluid is a function of both temperature and pressure. The pressure across the film thickness is commonly constant in hydrodynamic lubrication and boundary layer problems. In this analysis, however, the pressure is allowed to vary across the film thickness. The present analysis is applicable only to lubrication problems where the lubrication film thickness is much smaller than the flow length (small aspect ratio). Furthermore, the analysis is applicable only to flow between non-diverging plates. Modifications are needed so that shocks in converging–diverging spacings can be calculated.

The Newton–Raphson method is used to linearize the non-linear governing differential equations. The finite element method (FEM) is then used to solve the linearized boundary value problem. An 'upwind' finite element scheme is utilized since it helps the Newton–Raphson method to converge when the convective terms in the Navier–Stokes equations are significant. The results of this analysis are compared with (1) published results by Elrod and Chu[14] and (2) experimental results. Results obtained by the proposed method are also presented for an externally pressurized slider bearing. An externally pressurized slider bearing is defined as a slider bearing where the applied pressure at the entrance (stagnation pressure) is much higher than the

pressure at the exit (discharge pressure). Finally, the stiffness of an externally pressurized slider bearing is calculated for different geometrical characteristics of the bearing.

The motivation for this work was the development of an accurate flow analysis between two plates in order to (1) evaluate innovative ringless piston designs for low-heat-rejection (known also as 'adiabatic') engine applications and (2) develop an advanced gas film riding face seal which may replace conventional buffered labyrinth sealing systems which are used for sealing the compressor discharge air on current production gas turbine engines. The two-dimensional compressible Reynolds equation approach[15, 16] is not adequate since it does not account for the gas inertia effect. In an IC engine with a ringless piston, when the piston is close to the TDC position, the flow through the piston–linear interface accelerates rapidly until it reaches a Mach number equal to one (choked flow) for a non-divergent gap if the entrance Mach number is less than one. Choked flow is also encountered in gas film riding face seals for gas turbine engine applications. Therefore, the gas inertia effect represented by the convective terms of the Navier–Stokes equations is essential in this analysis.

HYDRODYNAMIC GAS FILM ANALYSIS

The steady state Navier–Stokes momentum equations and continuity equation for laminar, compressible flow of a Newtonian fluid using the notation of Figure 1 are as follows for an infinitely wide slider:

$$\rho\left(u\frac{\partial u}{\partial x}+w\frac{\partial u}{\partial z}\right)=-\frac{\partial p}{\partial x}+\frac{\partial}{\partial z}\left(\mu\frac{\partial u}{\partial z}\right), \tag{1a}$$

$$\rho\left(u\frac{\partial w}{\partial x}+w\frac{\partial w}{\partial z}\right)=-\frac{\partial p}{\partial z}+\frac{4}{3}\frac{\partial}{\partial z}\left(\mu\frac{\partial w}{\partial z}\right), \tag{1b}$$

$$\frac{\partial(\rho u)}{\partial x}+\frac{\partial(\rho w)}{\partial z}=0. \tag{2}$$

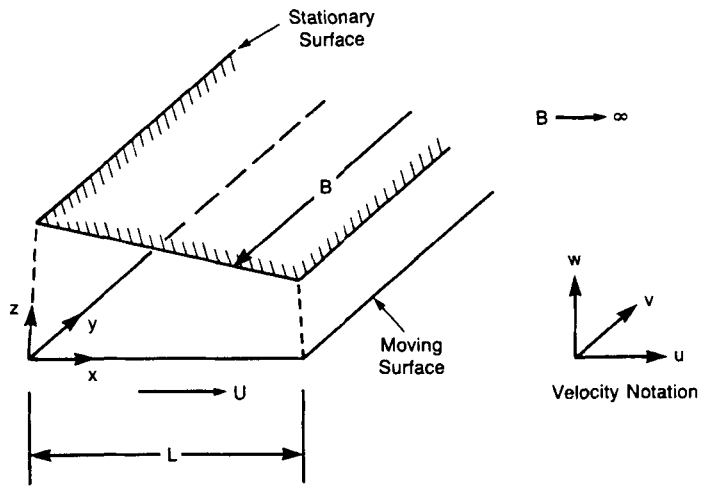

Figure 1. Bearing geometry and notation

In equations (1a) and (1b) the Stokes idealization ($2\mu+3\lambda=0$) is used and the body forces are assumed negligible for the lubricating film. Furthermore, the derivatives of the velocities across the film (z-direction) are assumed much greater than those in the direction of flow (x-direction). The equation of state for a perfect gas,

$$p=\rho RT, \tag{3}$$

relates the density to the pressure of the working fluid in this analysis. However, equation (3) introduces the temperature T as a new variable. The local gas temperature is determined by the following conservation of energy equation:

$$\rho\left(u\frac{\partial h_0}{\partial x}+w\frac{\partial h_0}{\partial z}\right)=\frac{\partial}{\partial z}\left(k\frac{\partial T}{\partial z}+\mu u\frac{\partial u}{\partial z}\right), \tag{4}$$

where h_0 is the stagnation fluid enthalpy. Under the general lubrication assumptions (boundary layer approximations), equation (4) is valid for a Newtonian fluid which obeys the Fourier conduction law.[14]

For a fluid with unit Prandtl number, equation (4) can be approximated by[14]

$$h_0=\text{constant}=h+u^2/2. \tag{5}$$

Equation (5) is the standard energy equation used in adiabatic, compressible gas flow calculations of a perfect gas.[17] For a perfect gas

$$h=c_pT=\frac{\gamma RT}{\gamma-1}.$$

Therefore equation (5) becomes

$$T_0=T+\frac{\gamma-1}{2\gamma R}u^2, \tag{6}$$

where T_0 is the stagnation fluid temperature. Equation (6) is used as an approximation of the energy equation (4) in this analysis. The local gas temperaure T is a function of the velocity u according to equation (6). This simplifies the present analysis because the gas temperature can be explicitly calculated from equation (6) if the velocity u is known. If the velocity u is much smaller than the local sonic velocity $c=\sqrt{(\gamma RT)}$, the gas temperaure T is practically equal to the stagnation temperature T_0 (isothermal film). However, if the gas velocity approaches the sonic velocity, T becomes very different from T_0.

The viscosity of the working fluid is a function of both temperature and pressure. The working fluid in this analysis is air. The viscosity of air at atmospheric pressure is given by the following regression equation:[18]

$$\mu=2{\cdot}5914\times10^{-15}T^3-1{\cdot}4346\times10^{-11}T^2+5{\cdot}0523\times10^{-8}T+4{\cdot}113\times10^{-6}\quad(\mathrm{N\,s\,m^{-2}}), \tag{7}$$

where T is the absolute temperature in Kelvin. By plotting equation (7), it can be seen that the viscosity varies almost linearly with temperature. In this analysis the air viscosity is assumed to be linear with temperature at atmospheric pressure as follows:

$$\mu=3{\cdot}8\times10^{-8}T+0{\cdot}6125\times10^{-5}\quad(\mathrm{N\,s\,m^{-2}}). \tag{8}$$

This linear relation approximates equation (7) very closely for practical purposes.

The variation of the viscosity of air with pressure at room temperature is given in Figure 2–3.2 of Reference 1. The viscosity increases linearly with increasing pressure with a slope of

$0{\cdot}41 \times 10^{-9}$ N s m^{-2} kPa^{-1}. In automotive diesel engine applications the maximum pressure of the working fluid can vary from atomospheric to approximately 13 800 kPa (2000 lbf in^{-2}). Therefore the inclusion of the variation of viscosity with pressure is essential in this analysis.

Finally, using equations (6) and (8), the variation of viscosity with velocity and pressure is as follows:

$$\mu = k_1 - k_2 u^2 + k_3 p \quad (\mathrm{N\,s\,m^{-2}}), \tag{9}$$

where

$$k_1 = 3{\cdot}8 \times 10^{-8} T_0 + 0{\cdot}6125 \times 10^{-5} \quad (\mathrm{N\,s\,m^{-2}}),$$

$$k_2 = 1{\cdot}891225 \times 10^{-11} \quad (\mathrm{N\,s^3\,m^{-4}}),$$

$$k_3 = 0{\cdot}41 \times 10^{-9} \quad (\mathrm{N\,s\,m^{-2}\,kPa^{-1}}),$$

and T_0 is in Kelvin.

The air constants γ and R are taken equal to 1·4 and 287·04 m^2 s^{-2} K^{-1} respectively. Equations (3) and (6) are used to eliminate the density ρ and the temperature T in equations (1) and (2) as follows:

$$\frac{p}{RT_0 - [(\gamma-1)/2\gamma]u^2}\left(u\frac{\partial u}{\partial x} + w\frac{\partial u}{\partial z}\right) = -\frac{\partial p}{\partial x} + \frac{\partial}{\partial z}\left((k_1 - k_2 u^2 + k_3 p)\frac{\partial u}{\partial z}\right), \tag{10a}$$

$$\frac{p}{RT_0 - [(\gamma-1)/2\gamma]u^2}\left(u\frac{\partial w}{\partial x} + w\frac{\partial w}{\partial z}\right) = -\frac{\partial p}{\partial z} + \frac{4}{3}\frac{\partial}{\partial z}\left((k_1 - k_2 u^2 + k_3 p)\frac{\partial w}{\partial z}\right), \tag{10b}$$

$$\frac{\partial}{\partial x}\left(\frac{pu}{RT_0 - [(\gamma-1)/2\gamma]u^2}\right) + \frac{\partial}{\partial z}\left(\frac{pw}{RT_0 - [(\gamma-1)/2\gamma]u^2}\right) = 0. \tag{11}$$

Equations (10) and (11) are solved simultaneously for (u, w, p).

The associated boundary conditions are (see notation of Figure 1)

$$u = U \quad \text{and} \quad w = 0 \quad \text{at } z = 0, \qquad u = 0 \quad \text{and} \quad w = 0, \quad \text{at } z = h. \tag{12}$$

At the entrance the velocity profile u can be specified. If a uniform entrance velocity u is assumed,

$$u = \bar{u}_{en} \quad \text{at } x = 0, \qquad w = 0 \quad \text{at } x = 0, \tag{13}$$

where $\bar{u}_{en}$ is the unknown constant velocity of the gas at the entrance. A uniform but unknown gas pressure p_{en} can also be assumed at the entrance. This pressure is determined by assuming an isentropic expansion of a perfect gas from the stagnation properties p_0, T_0 and $u_0 = 0$ to the gas properties p_{en}, T and $\bar{u}_{en}$ at the entrance:[17]

$$p_{en} = p_0\left(1 - \frac{\gamma-1}{2\gamma R T_0}\bar{u}_{en}^2\right)^{\gamma/(\gamma-1)}. \tag{14}$$

For non-choked flow conditions the pressure at the exit across the film thickness is equal to the atomospheric pressure p_a:

$$p = p_a \quad \text{at } x = L \quad \text{for non-choked flow.} \tag{15}$$

However, for choked flow the average gas velocity $\bar{u}_{ex}$ at the exit is taken equal to the sonic velocity c:

$$\bar{u}_{ex} = \frac{1}{h}\int_0^h u_{ex}\,dz = c \quad \text{at } x = L \quad \text{for choked flow.} \tag{16}$$

The pressure at the exit is unknown but greater than p_a.

The highly non-linear boundary value problem, which consists of equations (10a), (10b) and (11) and the boundary conditions of equations (12)–(14) and (15) or (16), is solved numerically for the unknowns u, w and p.

The Newton–Raphson method

The Newton–Raphson method is used to linearize equations (10) and (11) with respect to the unknowns u, w and p. Equations (10) and (11) can be rewritten in an operator form as

$$O(p, u, w)=0, \tag{17}$$

subject to the same boundary conditions as discussed previously. The Newton–Raphson method linearizes equation (17) as follows:

$$O(p_k, u_k, w_k)+O'(p_k, u_k, w_k)\Delta p_k+O'(p_k, u_k, w_k)\Delta u_k+O'(p_k, u_k, w_k)\Delta w_k=0, \tag{18}$$

where $O'(p_k, u_k, w_k)\Delta p_k$ is the Frechet derivative of $O(p_k, u_k, w_k)$ with respect to pressure at (p_k, u_k, w_k). Here k denotes the iteration index. If the Frechet derivative exists at (p_k, u_k, w_k), it is given by

$$O'(p_k, u_k, w_k)\Delta p_k=\lim_{a\to 0}\frac{\mathrm{d}}{\mathrm{d}a}O(p_k, u_k, w_k). \tag{19}$$

Similar expressions hold for $O'(p_k, u_k, w_k)\Delta u_k$ and $O'(p_k, u_k, w_k)\Delta w_k$. Equation (18) can be solved for the linear correction $(\Delta p_k, \Delta u_k, \Delta w_k)$, which in turn can be used to obtain a better estimate for the solution. If $(\Delta p_k, \Delta u_k, \Delta w_k)$ becomes progressively smaller as $k\to\infty$, then the sequence

$$p_{k+1}=p_k+\Delta p_k, \qquad u_{k+1}=u_k+\Delta u_k, \qquad w_{k+1}=w_k+\Delta w_k \tag{20}$$

converges to the solution. After some algebra, equation (18) can be written as

$$\begin{aligned}
&\left(u_k\frac{\partial(v_l)_k}{\partial x}+w_k\frac{\partial(v_l)_k}{\partial z}\right)\frac{\Delta p_k}{A-Bu_k^2}+\frac{\partial(\Delta p_k)}{\partial x_l}-\lambda_l\frac{\partial}{\partial z}\left(k_3\frac{\partial(v_l)_k}{\partial z}\Delta p_k\right)+\left[\frac{p_k}{A-Bu_k^2}\frac{\partial(v_l)_k}{\partial x}\right.\\
&\left.-\frac{2Bu_kp_k}{A-Bu_k^2}\left(u_k\frac{\partial(v_l)_k}{\partial x}+w_k\frac{\partial(v_l)_k}{\partial z}\right)\right]\Delta u_k+\frac{p_k}{A-Bu_k^2}\left(u_k\frac{\partial[\Delta(v_l)_k]}{\partial x}+\frac{\partial(v_l)_k}{\partial z}\Delta w_k+w_k\frac{\partial[\Delta(v_l)_k]}{\partial z}\right)\\
&-\lambda_l\frac{\partial}{\partial z}\left(-2k_2u_k\frac{\partial(v_l)_k}{\partial z}\Delta u_k+(k_1-k_2u_k^2+k_3p_k)\frac{\partial[\Delta(v_l)_k]}{\partial z}\right)\\
&=-\frac{p_k}{A-Bu_k^2}\left(u_k\frac{\partial(v_l)_k}{\partial x}+w_k\frac{\partial(v_l)_k}{\partial z}\right)-\frac{\partial p_k}{\partial x_l}+\lambda_l\frac{\partial}{\partial z}\left((k_1-k_2u_k^2+k_3p_k)\frac{\partial(v_l)_k}{\partial z}\right), \quad l=1, 2,
\end{aligned} \tag{21a}$$

$$\begin{aligned}
&\frac{\partial}{\partial x}\left(\frac{u_k\Delta p_k}{A-Bu_k^2}\right)+\frac{\partial}{\partial z}\left(\frac{w_k\Delta p_k}{A-Bu_k^2}\right)+\frac{\partial}{\partial x}\left[\left(-\frac{2Bu_k^2p_k}{(A-Bu_k^2)^2}+\frac{p_k}{A-Bu_k^2}\right)\Delta u_k\right]\\
&+\frac{\partial}{\partial z}\left(-\frac{2Bu_kw_kp_k}{(A-Bu_k^2)^2}\Delta u_k\right)+\frac{\partial}{\partial z}\left(\frac{p_k\Delta w_k}{A-Bu_k^2}\right)\\
&\qquad=-\frac{\partial}{\partial x}\left(\frac{p_ku_k}{A-Bu_k^2}\right)-\frac{\partial}{\partial z}\left(\frac{p_kw_k}{A-Bu_k^2}\right),
\end{aligned} \tag{21b}$$

where $A=RT_0$ and $B=(\gamma-1)/2\gamma$. In equation (21a), $l=1$ and $l=2$ correspond to the linearized momentum equations in the x- and z-directions respectively for the correction term

$(\Delta p_k, \Delta u_k, \Delta w_k)$. The notation for $l=1$ and $l=2$ is as follows:

$$v_1 = u, \quad x_1 = x \quad \text{and} \quad \lambda_1 = 1 \qquad (x\text{-direction}), \tag{22}$$

$$v_2 = w, \quad x_2 = z, \quad \text{and} \quad \lambda_2 = 4/3 \qquad (z\text{-direction}).$$

Equation (21b) represents the linearized continuity equation. The boundary conditions associated with equations (21) are

$$\Delta u_k = \Delta w_k = 0 \qquad \text{at } z = 0 \text{ or } h, \tag{23a}$$

$$\Delta u_k = \text{constant}, \quad \Delta p_k = \text{constant} \quad \text{and} \quad \Delta w_k = 0 \quad \text{at } x = 0, \tag{23b}$$

$$\Delta p_k + C\Delta u_k = -D \quad \text{at } x = 0, \tag{23c}$$

$$\Delta p_k = 0 \quad \text{at } x = L \quad \text{for non-choked flow}, \tag{23d}$$

where

$$C = p_{en} - p_0\left(1 - \frac{\gamma - 1}{2\gamma RT_0}\bar{u}_{en}^2\right)^{\gamma/(\gamma-1)},$$

$$D = \frac{p_0}{RT_0}\left(1 - \frac{\gamma - 1}{2\gamma RT_0}\bar{u}_{en}^2\right)^{1/(\gamma-1)}\bar{u}_{en}.$$

For choked flow the back pressure is varied until equation (16) is satisfied within practical tolerances.

Weak form

The exact, continuous solution of the boundary value problem of equations (21) and (23) is very difficult to obtain. Therefore a discrete approximation of the exact solution is found using the finite element method. A standard procedure of finite element methods in the solution of physical problems described by a boundary value problem is to change the boundary value problem to a so-called weak form. The weak form converts the strong local description of the problem (differential equations) to a weak global integral form by constructing an orthogonal projection of each of the residual spaces of the momentum and continuity equations onto a subspace spanned by appropriate weighting functions. This is achieved by multiplication of equations (21) by an arbitrary virtual correction term $\bar{n}_k$ (similar to virtual displacement in structural mechanics) and integration over the whole solution domain Ω.

The velocity virtual correction functions $\Delta\bar{u}_k$ and $\Delta\bar{w}_k$ and the pressure correction function $\Delta\bar{p}_k$ are used as the virtual correction term $\bar{n}_k$ for the momentum equations in the x- and z-directions and the continuity equation respctively.[19] Then integration by parts and use of the boundary conditions (23) yield

$$\int_\Omega \left(u_k\frac{\partial(v_l)_k}{\partial x} + w_k\frac{\partial(v_l)_k}{\partial z}\right)\frac{\Delta p_k}{A - Bu_k^2}\Delta(\bar{v}_l)_k\,d\Omega + \int_\Omega \left(\frac{\partial(\Delta p_k)}{\partial x_l}\Delta(\bar{v}_l)_k\,d\Omega\right.$$

$$+ \lambda_l\int_\Omega k_3\frac{\partial(v_l)_k}{\partial z}\Delta p_k\frac{\partial(\bar{v}_l)_k}{\partial z}\,d\Omega + \int_\Omega\left[\frac{p_k}{A - Bu_k^2}\frac{\partial(v_l)_k}{\partial x} - \frac{2Bu_kp_k}{(A - Bu_k^2)^2}\left(u_k\frac{\partial(v_l)_k}{\partial x}\right.\right.$$

$$\left.\left.+ w_k\frac{\partial(v_l)_k}{\partial z}\right)\right]\Delta u_k\Delta(\bar{v}_l)_k\,d\Omega + \int_\Omega\frac{p_k}{A - Bu_k^2}\left(u_k\frac{\partial[\Delta(v_l)_k]}{\partial x} + \frac{\partial(v_l)_k}{\partial z}\Delta w_k + w_k\frac{\partial[\Delta(v_l)_k]}{\partial z}\right)\Delta(\bar{v}_l)_k\,d\Omega$$

$$+\lambda_l \int_\Omega \left(-2k_2 u_k \frac{\partial (v_l)_k}{\partial z} \Delta u_k + (k_1 - k_2 u_k^2 + k_3 p_k) \frac{\partial [\Delta (v_l)_k]}{\partial z} \right) \frac{\partial [\Delta (\bar{v}_l)_k]}{\partial z} \mathrm{d}\Omega$$

$$= -\int_\Omega \frac{p_k}{A - Bu_k^2} \left(u_k \frac{\partial (v_l)_k}{\partial x} + w_k \frac{\partial (v_l)_k}{\partial z} \right) \Delta (\bar{v}_l)_k \, \mathrm{d}\Omega - \int_\Omega \frac{\partial p_k}{\partial x_l} \Delta (\bar{v}_l)_k$$

$$-\lambda_l \int_\Omega (k_1 - k_2 u_k^2 + k_3 p_k) \frac{\partial (v_l)_k}{\partial z} \frac{\partial [\Delta (\bar{v}_l)_k]}{\partial z} \mathrm{d}\Omega, \quad l = 1, 2, \tag{24a}$$

$$\int_\Omega \frac{u_k \Delta \bar{p}_k}{A - Bu_k^2} \frac{\partial (\Delta \bar{p}_k)}{\partial x} \mathrm{d}\Omega + \int_\Omega \frac{w_k \Delta p_k}{A - Bu_k^2} \frac{\partial (\Delta p_k)}{\partial z} \mathrm{d}\Omega + \int_\Omega \left(-\frac{2Bu_k^2 p_k}{(A - Bu_k^2)^2} + \frac{p_k}{A - Bu_k^2} \right) \Delta u_k \frac{\partial (\Delta \bar{p}_k)}{\partial x} \mathrm{d}\Omega$$

$$+\int_\Omega -\frac{2Bu_k w_k p_k}{(A - Bu_k^2)^2} \Delta u_k \frac{\partial (\Delta \bar{p}_k)}{\partial z} \mathrm{d}\Omega + \int_\Omega \frac{p_k \Delta w_k}{A - Bu_k^2} \frac{\partial (\Delta \bar{p}_k)}{\partial z} \mathrm{d}\Omega$$

$$= -\int_\Omega \frac{p_k u_k}{A - Bu_k^2} \frac{\partial (\Delta \bar{p}_k)}{\partial x} \mathrm{d}\Omega - \int_\Omega \frac{p_k w_k}{A - Bu_k^2} \frac{\partial (\Delta \bar{p}_k)}{\partial z} \mathrm{d}\Omega. \tag{24b}$$

All the boundary terms from the integration by parts are equal to zero for non-choked flow because of the boundary conditions (23).

Finite element discretization

Serious attention must be given to the choice of interpolation functions for the velocity components and the pressure. Several different approaches have established that the interpolation functions for the velocity components should be one order higher than the pressure interpolation functions. Yamada *et al.*[20] arrived at this conclusion through consideration of a variational formula. Hood and Taylor[21] arrived at the same conclusion directly by considering errors in the weighted residual formulation, and Olson and Tuann[22] showed that spurious rigid-body modes occur in the element coefficient matrix unless this condition is met. Bercovier and Pironneau[23] have confirmed the conclusion through a rigorous mathematical study of error estimates for Stokes flow. Typical finite elements for viscous flow maintain C^0-continuity for the velocity components and the pressure but use interpolation functions for velocities one degree higher than pressure. This means that there are more velocity unknowns than pressure unknowns.

The solution domain Ω is divided in this study into E quadrilateral elements as in Figure 2. The area of each element is denoted by Ω_e. The nine-node Lagrangian (subparametric) parabolic element is used for the discretization of both the velocity components. However, the four-node, linear, isoparametric element is used for the pressure discretization. An automatic mesh generator was developed which provides the co-ordinates of each node and the connectivities for both the velocity and the pressure elements. More points can be placed at the inlet and exit of the bearing in the direction of the flow (x-direction). This provides a dense grid in the regions where the gas inertia effect is more profound. The mesh generator can also create a dense grid close to the two bearing boundaries in the z-direction. This is necessary because the velocity gradient in the z-direction is large owing to the considerable viscous flow effect close to the walls which confine the flow. Furthermore, the mesh generator uses a node-numbering pattern which minimizes the bandwidth of the system of equations during the solution process, reducing the computational cost substantially.

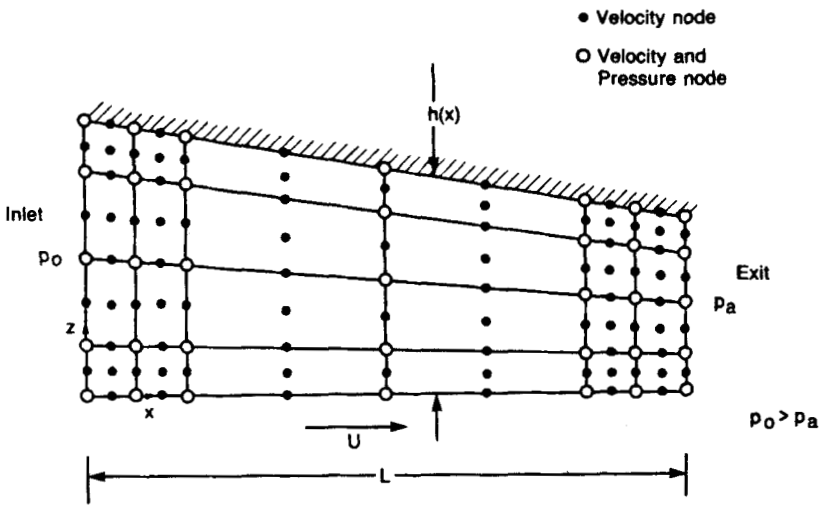

Figure 2. Geometry and discretization of flow domain

The nine-node velocity element is shown in Figure 3. Within each nine-node Lagrangian element the velocity corrections Δu_k and Δw_k are approximated as follows:

$$\Delta u_k(x, z) = \sum_{i=1}^{9} N_i^{\nu}(\xi, \eta)\Delta u_{k_i}, \tag{25a}$$

$$\Delta w_k(x, z) = \sum_{i=1}^{9} N_i^{\nu}(\xi, \eta)\Delta w_{k_i}. \tag{25b}$$

The interpolation (shape) functions N_i^{ν} are[24]

$$\begin{aligned}
&N_1^{\nu}(\xi,\eta)=L_1(\xi)L_1(\eta), && N_2^{\nu}(\xi,\eta)=L_2(\xi)L_1(\eta), && N_3^{\nu}(\xi,\eta)=L_3(\xi)L_1(\eta),\\
&N_4^{\nu}(\xi,\eta)=L_3(\xi)L_2(\eta), && N_5^{\nu}(\xi,\eta)=L_3(\xi)L_3(\eta), && N_6^{\nu}(\xi,\eta)=L_2(\xi)L_3(\eta),\\
&N_7^{\nu}(\xi,\eta)=L_1(\xi)L_3(\eta), && N_8^{\nu}(\xi,\eta)=L_1(\xi)L_2(\eta), && N_9^{\nu}(\xi,\eta)=L_2(\xi)L_2(\eta),
\end{aligned} \tag{26}$$

where

$$\begin{aligned}
&L_1(\xi)=\tfrac{1}{2}\xi(\xi-1), && L_2(\xi)=1-\xi^2, && L_3(\xi)=\tfrac{1}{2}\xi(\xi+1),\\
&L_1(\eta)=\tfrac{1}{2}\eta(\eta-1), && L_2(\eta)=1-\eta^2, && L_3(\eta)=\tfrac{1}{2}\eta(\eta+1).
\end{aligned} \tag{27}$$

The Galerkin finite element method has been used extensively to solve fluid flow problems. The Galerkin method uses the interpolation functions N_i^{ν} as the weighting functions W_i. However, spurious oscillations have been encountered with the Galerkin method when convective (first-derivative) terms are significant and therefore an elliptic boundary value problem with dominant first-derivative terms is to be solved. This problem is common in Navier–Stokes flows at high Reynolds number and convective transport phenomena at moderate to high Peclet number. The oscillations can only be removed by severe mesh refinement, which undermines the practical utility of the Galerkin method. An alternative approach is to use 'upwind' finite elements or, equivalently, a Petrov–Galerkin method with weighting functions W_i different from the interpolation functions N_i.[25–27] In this study, 'upwind' finite elements are used for the velocity

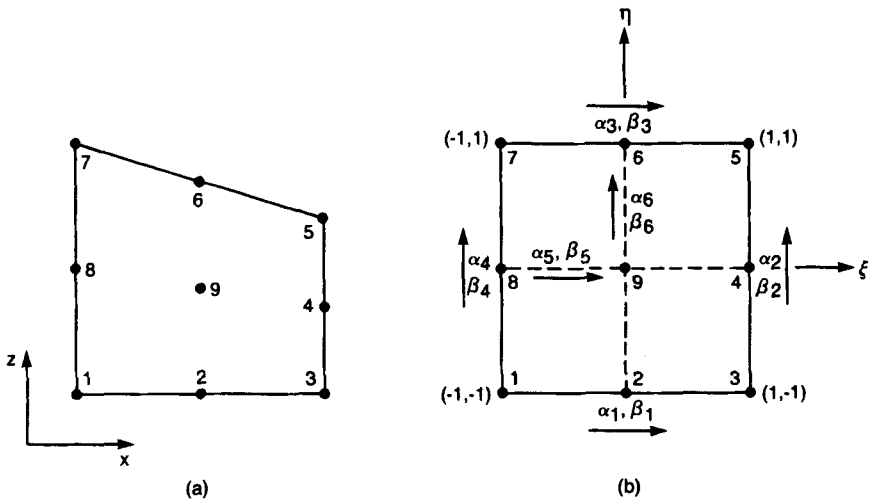

Figure 3. Natural co-ordinates for nine-node quadrilateral Lagrangian element: (a) Cartesian co-ordinates; (b) natural co-ordinates. Element coefficients and positive velocity directions

approximations since viscous flow at high Reynolds number with dominant convective terms (inertia effect) is considered. The weighting functions for the nine-node Lagrangian parabolic element in the natural co-ordinate system (ξ, η) are chosen as follows:[26]

$$
\begin{aligned}
W_1(\xi,\eta) &= [L_1(\xi)-\alpha_1 F(\xi)][L_1(\eta)-\alpha_4 F(\eta)],\\
W_2(\xi,\eta) &= [L_2(\xi)+4\beta_1 F(\xi)][L_1(\eta)-\alpha_6 F(\eta)],\\
W_3(\xi,\eta) &= [L_3(\xi)-\alpha_1 F(\xi)][L_1(\eta)-\alpha_2 F(\eta)],\\
W_4(\xi,\eta) &= [L_3(\xi)-\alpha_5 F(\xi)][L_2(\eta)+4\beta_2 F(\eta)],\\
W_5(\xi,\eta) &= [L_3(\xi)-\alpha_3 F(\xi)][L_3(\eta)-\alpha_2 F(\eta)],\\
W_6(\xi,\eta) &= [L_2(\xi)+4\beta_3 F(\xi)][L_3(\eta)-\alpha_6 F(\eta)],\\
W_7(\xi,\eta) &= [L_1(\xi)-\alpha_3 F(\xi)][L_3(\eta)-\alpha_4 F(\eta)],\\
W_8(\xi,\eta) &= [L_1(\xi)-\alpha_5 F(\xi)][L_2(\eta)+4\beta_4 F(\eta)],\\
W_9(\xi,\eta) &= [L_2(\xi)+4\beta_5 F(\xi)][L_2(\eta)+4\beta_6 F(\eta)],
\end{aligned}
\tag{28}
$$

where

$$F(\xi)=\tfrac{5}{8}\xi(\xi+1)(\xi-1), \tag{29a}$$

$$F(\eta)=\tfrac{5}{8}\eta(\eta+1)(\eta-1). \tag{29b}$$

The coefficients α and β in equations (28) are taken as[26]

$$\alpha = 1-2/\gamma, \tag{30}$$

$$\beta = 1-4/\gamma, \tag{31}$$

where

$$\gamma = \left|\frac{uh\rho}{\mu}\right|. \tag{32}$$

To compute the coefficients for a side joining nodes i and j, where i and j are both corner nodes, the velocity u in equation (32) is the mean velocity in the direction of this side. The positive velocity directions are indicated by arrows in Figure 3. The sign of the mean velocity u determines the sign of the coefficients α and β. In equation (32), h is the length between nodes i and j, and ρ and μ are the fluid average density and average viscosity respectively along the side connecting nodes i and j. Within each nine-node velocity element the virtual velocity corrections $\Delta\bar{u}_k$ and $\Delta\bar{w}_k$ (see equations (24a) for $l=1$ and $l=2$ respectively) are approximated as follows:

$$\Delta\bar{u}_k(x, z)=\sum_{j=1}^{9} W_j(\xi, \eta)\Delta\bar{u}_{k_j}, \tag{33a}$$

$$\Delta\bar{w}_k(x, z)=\sum_{j=1}^{9} W_j(\xi, \eta)\Delta\bar{w}_{k_j}, \tag{33b}$$

The four-node isoparametric element is used for the pressure discretization. The four nodes of this element are the same as the corner nodes of the corresponding nine-node Lagrangian velocity element (see Figure 2). Within each pressure element the pressure correction Δp_k and the virtual pressure correction $\Delta\bar{p}_k$ (see equations (24)) are approximated as follows:

$$\Delta p_k(x, z)=\sum_{i=1}^{4} N_i^P(\xi, \eta)\Delta p_{k_i}, \tag{34a}$$

$$\Delta\bar{p}_k(x, z)=\sum_{j=1}^{4} N_i^P(\xi, \eta)\Delta\bar{p}_{k_j}. \tag{34b}$$

Note that the weighting functions are the same as the interpolation functions N_i^P for the pressure finite elements. The interpolation functions N_i^P are as follows in the natural co-ordinate system (ξ, η):[24]

$$\begin{aligned} N_1^P(\xi, \eta)&=\tfrac{1}{4}(1-\xi)(1-\eta), & N_2^P(\xi, \eta)&=\tfrac{1}{4}(1+\xi)(1-\eta),\\ N_3^P(\xi, \eta)&=\tfrac{1}{4}(1+\xi)(1+\eta), & N_4^P(\xi, \eta)&=\tfrac{1}{4}(1-\xi)(1+\eta). \end{aligned} \tag{35}$$

It is apparent from the chosen virtual correction functions $\Delta\bar{u}_k$, $\Delta\bar{w}_k$, and $\Delta\bar{p}_k$ that the Petrov–Galerkin method is used to find the weak form of the momentum equations (24a), while the Galerkin method is used to find the weak form of the continuity equation (24b).

Fluidity matrix and load vector

The fluidity matrix and the generalized load vector are obtained from the weak form of the momentum equations and continuity equation (equations (24)) using the discretization discussed in the previous section. Substitution of the approximation functions of equations (25), (33) and (34) in equations (24) yields

$$\begin{aligned} &\sum_{e=1}^{E}\Delta(\bar{v}_l)_{k_j}\left\{\int_{\Omega_e}\left(u_k\frac{\partial(v_l)_k}{\partial x}+w_k\frac{\partial(v_l)_k}{\partial z}\right)W_j\frac{N_i^P}{A-Bu_k^2}\,d\Omega+\int_{\Omega_e}W_j\frac{\partial(N_i^P)}{\partial x_l}\,d\Omega\right.\\ &\left.+\lambda_l\int_{\Omega_e}k_3\frac{\partial(v_l)_k}{\partial z}\frac{\partial W_j}{\partial z}N_i^P\,d\Omega\right\}\Delta p_{k_i}+\sum_{e=1}^{E}\Delta(\bar{v}_l)_{k_j}\left\{\int_{\Omega_e}\left[\frac{p_k}{A-Bu_k^2}\frac{\partial(v_l)_k}{\partial x}\right.\right.\\ &\left.\left.-\frac{2Bu_kp_k}{(A-Bu_k^2)^2}\left(u_k\frac{\partial(v_l)_k}{\partial x}+w_k\frac{\partial(v_l)_k}{\partial z}\right)\right]W_jN_i^v\,d\Omega\right. \end{aligned}$$

$$+\lambda_l \int_{\Omega_e} -2k_2 u_k \frac{\partial (v_l)_k}{\partial z} \frac{\partial W_j}{\partial z} N_i^v \, d\Omega \Big\} \Delta u_{k_i}$$

$$+ \sum_{e=1}^{E} \Delta(\bar{v}_l)_{k_j} \Big\{ \int_{\Omega_e} \frac{p_k}{A - Bu_k^2} W_j \frac{\partial (v_l)_k}{\partial z} N_i^v \, d\Omega \Big\} \Delta w_{k_i}$$

$$+ \sum_{e=1}^{E} \Delta(\bar{v}_l)_{k_j} \Big\{ \int_{\Omega_e} \frac{p_k}{A - Bu_k^2} W_j \Big(u_k \frac{\partial (N_i^v)_k}{\partial x} + w_k \frac{\partial (N_i^v)_k}{\partial z} \Big) d\Omega$$

$$+\lambda_l \int_{\Omega_e} (k_1 - k_2 u_k^2 + k_3 p_k) \frac{\partial W_j}{\partial z} \frac{\partial (N_i^v)}{\partial z} d\Omega \Big\} \Delta (v_l)_{k_i}$$

$$= \sum_{e=1}^{E} \Delta(\bar{v}_l)_{k_j} \Big\{ - \int_{\Omega_e} \frac{p_k}{A - Bu_k^2} \Big(u_k \frac{\partial (v_l)_k}{\partial x} + w_k \frac{\partial (v_l)_k}{\partial z} \Big) W_j \, d\Omega$$

$$- \int_{\Omega_e} \frac{\partial p_k}{\partial x_l} W_j \, d\Omega - \lambda_l \int_{\Omega_e} (k_1 - k_2 u_k^2 + k_3 p_k) \frac{\partial (v_l)_k}{\partial z} \frac{\partial W_j}{\partial z} d\Omega \Big\}, \quad l = 1, 2, \tag{36a}$$

where $l=1$ and $l=2$ correspond to the momentum equations in the x- and z-directions respectively and

$$\sum_{e=1}^{E} \Delta \bar{p}_{k_j} \Big\{ \int_{\Omega_e} \frac{u_k}{A - Bu_k^2} \frac{\partial (N_j^p)}{\partial x} N_i^p \, d\Omega + \int_{\Omega_e} \frac{w_k}{A - Bu_k^2} \frac{\partial (N_j^p)}{\partial z} N_i^p \, d\Omega \Big\} \Delta p_{k_i}$$

$$+ \sum_{e=1}^{E} \Delta \bar{p}_{k_j} \Big\{ \int_{\Omega_e} \Big(- \frac{2Bu_k^2 p_k}{(A - Bu_k^2)^2} + \frac{p_k}{A - Bu_k^2} \Big) \frac{\partial (N_j^p)}{\partial x} N_i^v \, d\Omega + \int_{\Omega_e} - \frac{2Bu_k w_k p_k}{(A - Bu_k^2)^2} \frac{\partial (N_j^p)}{\partial z} N_i^v \, d\Omega \Big\} \Delta u_{k_i}$$

$$+ \sum_{e=1}^{E} \Delta \bar{p}_{k_j} \Big\{ \int_{\Omega_e} \frac{p_k}{(A - Bu_k^2} \frac{\partial (N_j^p)}{\partial z} N_i^v \, d\Omega \Big\} \Delta w_{k_i}$$

$$= \sum_{e=1}^{E} \Delta \bar{p}_{k_j} \Big\{ - \int_{\Omega_e} \frac{p_k u_k}{A - Bu_k^2} \frac{\partial (N_j^p)}{\partial x} d\Omega - \int_{\Omega_e} \frac{p_k u_k}{A - Bu_k^2} \frac{\partial (N_j^p)}{\partial z} d\Omega \Big\}. \tag{36b}$$

The expressions in large braces on the LHS and RHS of equations (36) are parts of the element fluidity matrix and the element load vector respectively. The assembling of the element fluidity matrices and load vectors is indicated by the summation signs in the above equations. After the assembling, the virtual correction functions $\Delta \bar{p}_k$ and $\Delta(\bar{v}_l)_k$, $l=1, 2$ (or equivalently $\Delta \bar{u}_k$ and $\Delta \bar{w}_k$), cancel out in equations (36) since they appear on both the RHS and LHS of the equations and at the same time are arbitrary functions which only satisfy the boundary conditions. Equations (36) represent the assembled fluidity matrix and load vector for all three correction functions ($\Delta \bar{p}_k$, $\Delta \bar{u}_k$, $\Delta \bar{w}_k$) in a coupled form. Solution of these linear equations gives all three unknown correction functions at each nodal point for the kth iteration of the Newton–Raphson iterative solution procedure. On average, four to seven iterations are needed for the Newton–Raphson procedure to converge.

The partial derivatives of the interpolation functions with respect to x and z, appearing in the element fluidity matrices and load vectors in equations (36), are calculated by using the element Jacobian matrix. The area integrations in the element fluidity matrices and load vectors are performed using a nine-point Gaussian quadrature formula.[24] The global fluidity matrix is unsymmetric but banded. For this reason the Gaussian elimination method for unsymmetric but banded matrices is used to solve the system of linear equations for each Newton–Raphson iteration step.

VERIFICATION OF THE MODEL

The accuracy of the developed method is checked against (1) published r esults by Elrod and Chu[14] on the inertia and energy effects in the developing gas film between two parallel plates and (2) the measured flow of a compressible fluid between two parallel plates.

Comparison with results of Elrod and Chu

Elrod and Chu[14] studied the inertia and temperature effects in entrance flow between parallel flat plates using the boundary layer theory. In addition, they developed an approximate theory which is implemented by a 'gas table' similar to that employed for conventional Fanno-line computations.

In Table I of Reference 14 the authors present the pressure–distance relation in developing laminar flow with entrance Mach number $M_{en}=0{\cdot}2$. They present the non-dimensional pressure p/p_0 as a function of the non-dimensional distance xv_0/a^2U from the bearing entrance, where p_0 is the stagnation pressure of the entering flow, v_0 is the kinematic viscosity of the working fluid at the entrance stagnation state, a is the halfwidth between the two parallel plates ($a=h/2$), U is the average entrance velocity of the fluid and x is the distance from the entrance of the flow. The flow of air between two parallel plates of length $L=10$ mm is calculated using the present analysis and compared with the results given by Elrod and Chu[14] for $M_{en}=0{\cdot}2$. The stagnation pressure of the entering flow, p_0, is kept constant at 3450 kPa (500 lbf in^{-2}), while the back pressure (pressure at the exit) is varied until an entrance Mach number $M_{en}=0{\cdot}2$ is reached. The air stagnation temperature is 25 °C. The results of the present analysis are compared with the results from Elrod

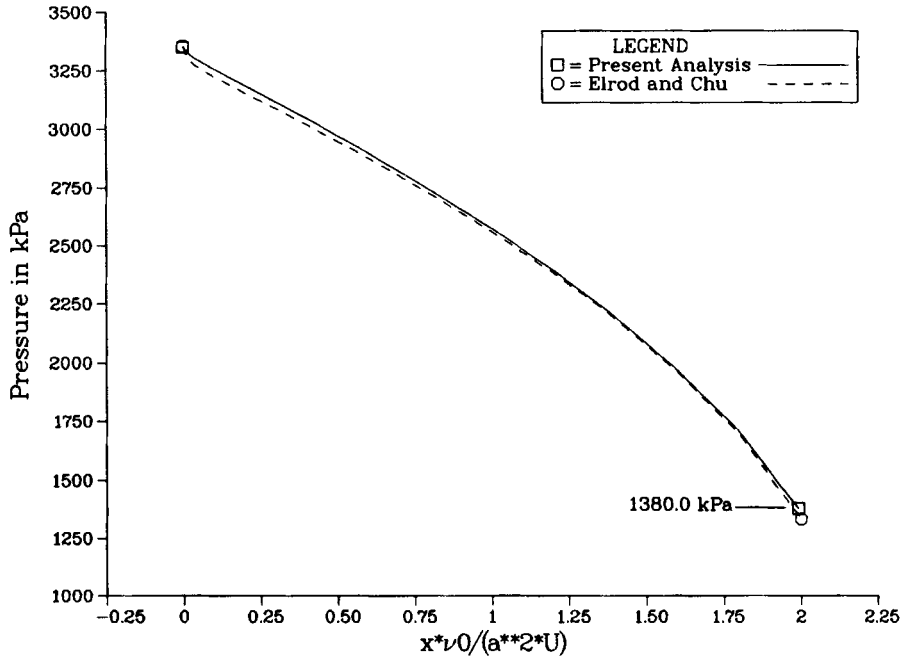

Figure 4. Pressure distribution between two parallel plates with $h=11$ μm, $L=10$ mm, $p_0=3450$ kPa, $T_0=25$ °C and $M_{en}=0.2$

and Chu's analysis in Figure 4 for $h = 11$ μm. The present analysis compares very well with Elrod and Chu's analysis.

Next, a comparison is performed between the present analysis and that of Elrod and Chu[14] in order to demonstrate the accuracy of the present analysis in calculating the flow between two parallel plates for choked flow conditions. The stagnation pressure and temperature at the entrance are $p_0 = 3450$ kPa and $T_0 = 200\,^{\circ}$C respectively. The results are presented in Table I. In order to demonstrate the importance of the fluid inertia effect in calculating the flow accurately, the compressible Reynolds equation approach (see Appendix I), which neglects the fluid inertia effect, is used and its results are also presented in Table I.

Although the present analysis compares very well with Elrod and Chu's analysis, the compressible Reynolds equation gives a very different flow. From these results and many other numerical experiments it was concluded that for choked flow or for non-choked flow with relatively high exit Mach number ($M_{ex} > 0{\cdot}5$–$0{\cdot}7$) the present analysis is necessary if the flow is to be calculated accurately.

Comparison with experimental data

An experimental study of air flow between two parallel plates was conducted at the General Motors Research Laboratories in the early 1960s. This study was prompted by the increasing interest in externally pressurized (pneumostatic) gas bearings at that time for use in numerous specialized applications.

The measured flow rates are presented in Table II for different operating conditions (clearance, flow width, inlet pressure, back pressure and stagnation temperature). The flow path length (bearing length) is 13·31 mm for all the operating conditions in Table II. In the same table the calculated flow rates with the present analysis and with the compressible Reynolds equation method of Appendix I are also presented. In the last two columns of Table II the percentage deviation of the calculated results from the measured results is presented. For relatively low velocity flows due to either small clearance (first and second rows of Table II) or moderate clearance and small inlet pressure (fourth row of Table II), both the present analysis and the compressible Reynolds equation method compare very well with the measured flow. In this case the compressible Reynolds equation gives good results because the gas inertia effect is negligible due to low-velocity flows. However, for high-velocity flows due to moderate clearance and high inlet pressure (third row of Table II) or large clearance (last four rows of Table II), the present analysis compares very well with the experimental results while the compressible Reynolds equation is very much in error.

Table I. Calculation of the choked flow between two parallel plates with $h = 14$ μm, $L = 10$ mm, $p_0 = 3450$ kPa and $T_0 = 200\,^{\circ}$C

	Elrod and Chu[14]	Present analysis	Compressible Reynolds equation
p_{en} (kPa)	3355·12	3349·12	3306·48
p_{ex} (kPa)	774·73	759·0	800·4
M_{en}	0·2	0·205	0·25
M_{ex}	1·0	1·0	1·0
Flow ($g\,s^{-1}$)	6·254	5·904	7·547

Table II. Comparison of experimental flow data with calculated flow data for bearing length $L = 13{\cdot}31$ mm

h (μm)	Flow width (mm)	p_0 (kPa)	p_a (kPa)	T_0 (°C)	Measured flow q_m from Reference 9 ($g\,s^{-1}$)	Present analysis flow q_p ($g\,s^{-1}$)	Compressible Reynolds equation flow q_r as in Appendix I ($g\,s^{-1}$)	$\frac{q_p - q_m}{q_m} \times 100$ (%)	$\frac{q_r - q_m}{q_m} \times 100$ (%)
13·51	101·19	512·47	98·8	26·77	0·124	0·128	0·131	3·22	5·64
13·31	101·19	236·46	98·53	26·55	0·0236	0·0225	0·0229	−4·66	−2·96
25·7	113·78	512·96	107·08	22·77	0·884	0·89	1·03	0·67	16·51
25·47	113·78	200·66	99·23	23·05	0·118	0·119	0·121	0·84	2·54
52·67	103·26	375·02	103·76	28·88	1·97	1·95	3·07	−1·01	55·83
52·54	103·26	237·02	101·05	28·88	1·07	1.04	1·27	−2·8	18·69
52·54	103·26	200·45	100·11	29·16	0·786	0·791	0·86	0·63	9·41
104·36	26·48	374·48	101·52	24·77	1·65	1·53	2·08	−7·27	26·06

SELECTED RESULTS

In this section the flow between two non-parallel plates representing a slider bearing, is calculated with the present method for certain operating conditions. The bearing length is $L = 12$ mm and the stagnation pressure and temperature at the bearing entrance are $p_0 = 3450$ kPa and $T_0 = 200\,^{\circ}C$ respectively.

Figures 5–7 show the distribution of the axial velocity $u(x, z)$ for choked flow when the plates are stationary ($U = 0$). The film thickness at the entrance and exit is $h_1 = 20\ \mu$m and $h_2 = 10\ \mu$m respectively. The atomospheric pressure $p_a = 103$ kPa is applied at the exit. The uniform velocity

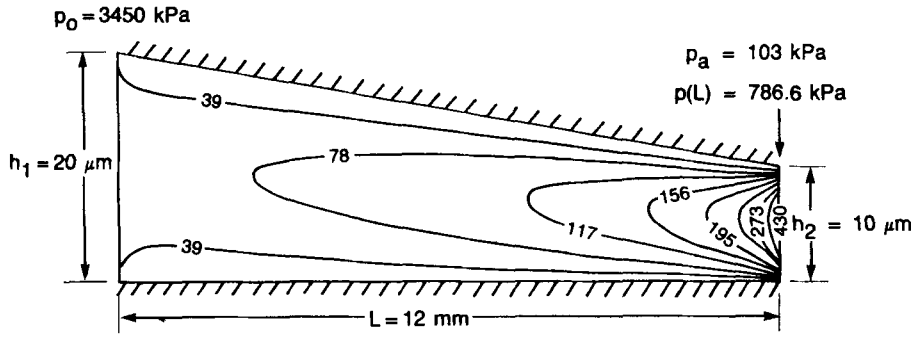

Figure 5. Distribution of velocity $u(x, z)$ in metres per second for choked flow between two non-parallel but stationary plates with uniform entrance velocity

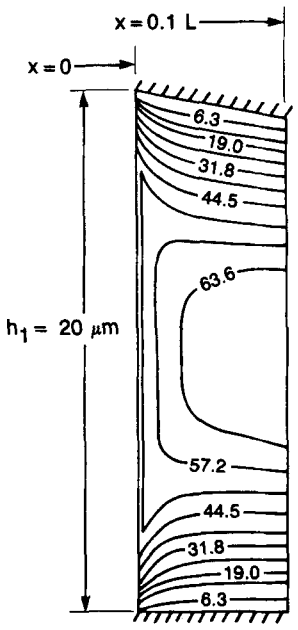

Figure 6. Distribution of velocity $u(x, z)$ in metres per second for choked flow between two non-parallel but stationary plates with uniform entrance velocity for $0 \leqslant x \leqslant 0{\cdot}1L$

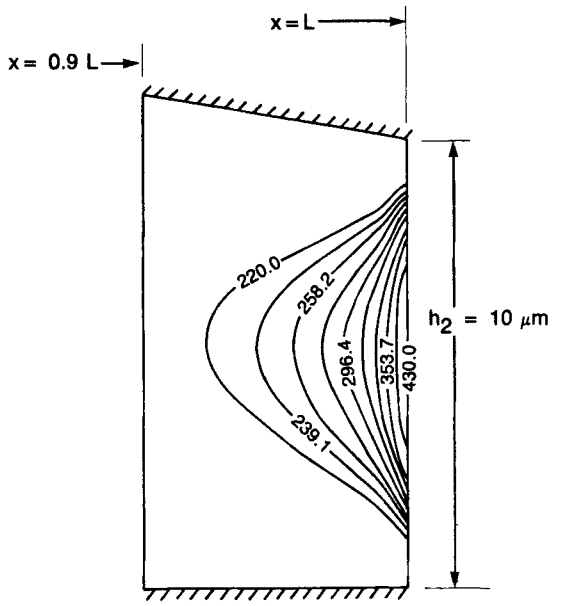

Figure 7. Distribution of velocity $u(x, z)$ in metres per second for choked flow between two non-parallel but stationary plates with uniform entrance velocity for $0{\cdot}9L \leqslant x \leqslant L$

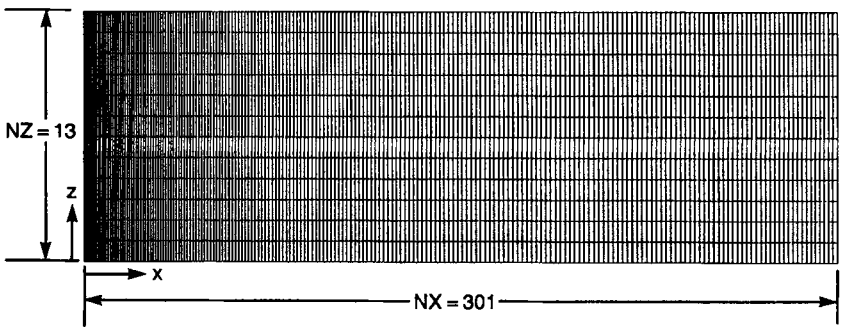

Figure 8. Computational grid for flow between two plates with uniform entrance velocity

assumption has been imposed at the bearing entrance. The computational grid used in this example is shown in Figure 8. $NX = 301$ was used in the x-direction and $NZ = 13$ was used in the z-direction. As shown in Figure 5, the flow is slow in the first half of the bearing while it accelerates rapidly at the exit (Figures 5 and 7). The formation of a laminar boundary layer at the bearing entrance is clearly shown in Figure 6. The boundary layer is fully developed for $x > 0{\cdot}025L$. Away from the entrance the velocity distribution across the film gap is almost parabolic. This type of flow in the entry region of a bearing or a tube due to uniform entrance velocity is well observed and mentioned in the literature (e.g. see Figures 1–10 in Referece 28). Because of the very rapid changes of the velocity profile in the entrance region, a very find grid is required in the axial direction close to the entrance in order for the computational scheme to converge. This is done by an automatic mesh generator.

Close to the bearing exit the flow accelerates very rapidly (Figures 5 and 7) due to a sharp pressure gradient at the bearing exit (Figure 10). The flow velocity goes from Mach number 0·5 at $x=0{\cdot}925L$ to Mach number 1·0 (choked flow) at $x=L$ (Figure 7). At the exit the critical pressure is $p(L)=786{\cdot}6$ kPa (Figure 10). Recall that the atmospheric pressure $P_a=103$ kPa is applied at the bearing exit.

Owing to the rapid flow acceleration, a finer mesh is also needed at the bearing exit in order to calculate the flow accurately. However, several numerical experiments with the present analysis have shown that computational accuracy at the entrance is much more important than the computational accuracy at the exit for convergence of the algorithm. For this reason, when the uniform entrance velocity assumption is used, a dense grid is used only around the entrance while a relatively coarse grid is used along the rest of the bearing length, including the exit area. This reduces the computational cost substantially and at the same time ensures convergence of the algorithm.

It was also found that when the uniform entrance velocity assumption is removed, the pressure distribution along the bearing is virtually unaffected. Furthermore, the flow pattern in the bearing is also unaffected after the laminar boundary layer is fully developed. Therefore the assumption of the shape of the entrance velocity is not expected to affect the flow very much for the applications appearing in this paper.

The influence of the energy equation in calculating the flow is demonstrated in Figures 9 and 10. If the energy equation is considered in the analysis, the velocity of the flow is coupled with the temperature of the working fluid at a particular (x, z)-position. Therefore, if air is the working fluid, the fluid viscosity varies according to equation (9) depending on the axial velocity $u(x, z)$. The results with the energy equation considered in the analysis are denoted by the broken lines

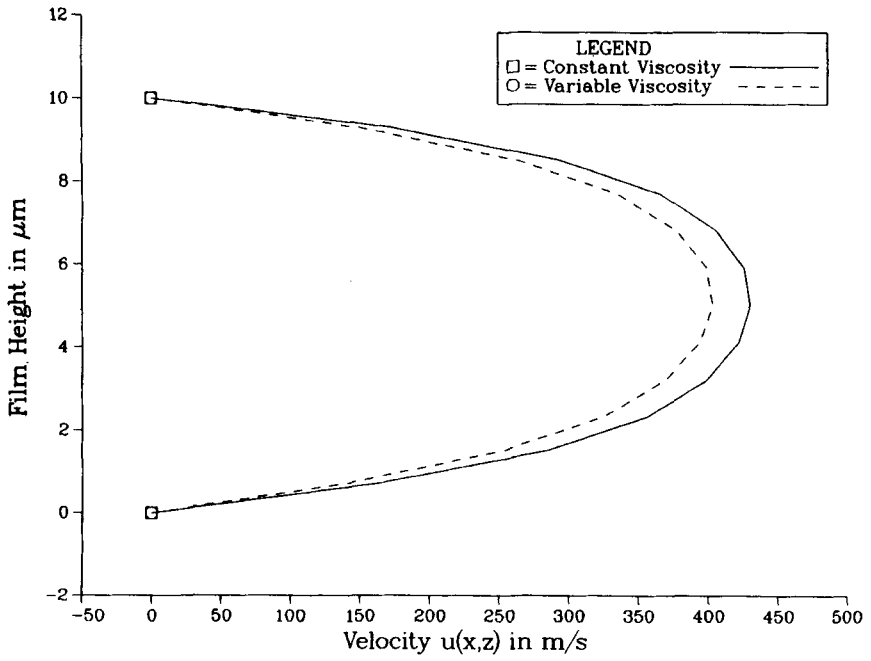

Figure 9. Velocity distribution at bearing exit for flow between two non-parallel plates

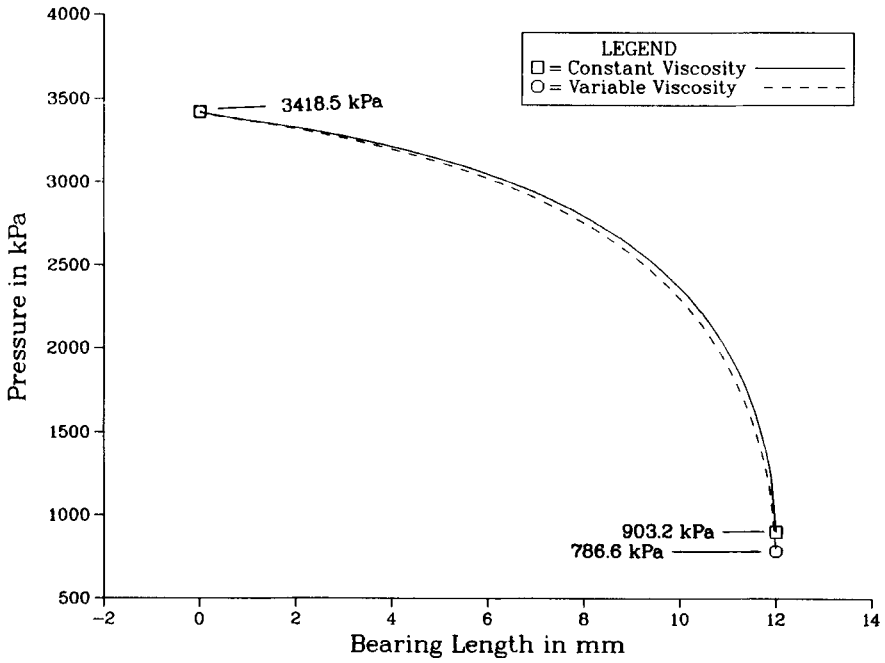

Figure 10. Pressure distribution along bearing for choked flow between two non-parallel plates

(variable viscosity) in Figures 9 and 10. The solid lines in the same figures represent the results when the fluid viscosity is independent of the fluid velocity (constant viscosity). The geometry and operating conditions here are the same unless specified otherwise. The solid line in Figure 9 represents the velocity at the bearing exit for choked flow with constant viscosity. As shown in Figure 10, the critical pressure is $p(L)=903{\cdot}2$ kPa. Recall that the critical pressure is $p(L)=786{\cdot}6$ kPa when the energy equation is used. If the exit pressure $p(L)=903{\cdot}2$ kPa is imposed as a boundary condition with the energy equation considered in the analysis (variable viscosity), the velocity at the exit is given by the broken line in Figure 9. It is noted that for variable viscosity the velocity at the exit is less than the velocity obtained with constant viscosity. This means that the critical pressure will be higher when the energy equation is not considered (Figure 10) in order to compensate for the flow deceleration at the exit. Figure 10 compares the pressure distribution for choked flow between the constant viscosity and variable viscosity cases. For practical applications the pressure distribution does not change considerably. It was also found that the maximum velocity (occurring around the midspan position) at cross-sections along the bearing length is only 6% higher when a variable viscosity is used compared to the constant viscosity case. From these results it is concluded that the energy equation can be omitted in most of the practical applications considered in this paper.

Figure 11 compares the axial pressure distribution and midspan velocity obtained with the present analysis and the Reynolds equation approach. When the inertia effect is neglected (Reynolds equation), the calculated pressure is underestimated while the flow velocity is substantially overestimated. The overestimation of the velocity introduced an almost 50% error in the flow for this example. This error increases with increasing inclination angle of the slider bearing, indicating that the gas inertia effect is more profound for large inclination angles.

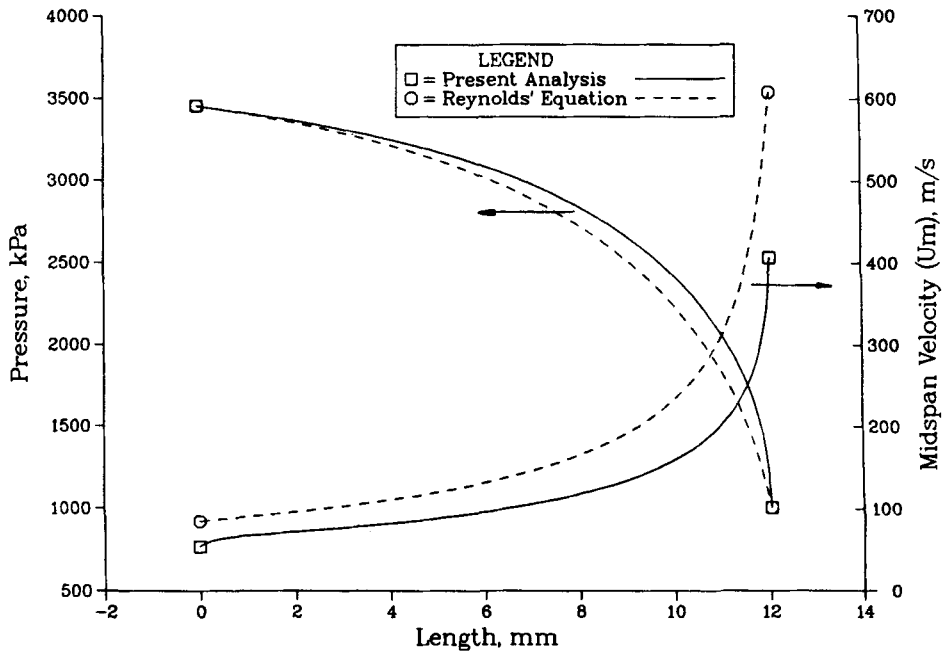

Figure 11. Comparison of pressure and midspan velocity distributions between present analysis and Reynolds equation approach

Figure 12 illustrates the influence of the relative motion between the two planes on the pressure and velocity distributions. The lower plane is moving with a velocity $U = 127{\cdot}0$ or $254{\cdot}0\ \mathrm{m\,s^{-1}}$. Positive U means that the lower plate moves in the same direction as the flow. The rest of the operating conditions are the same. A small relative velocity U does not affect the Poisseuille flow between the two planes especially for high-Mach-number flow. However, for $U = 127{\cdot}0$ or $254{\cdot}0\ \mathrm{m\,s^{-1}}$ the influence of U is considerable. Note that the sonic velocity for air is $429{\cdot}0\ \mathrm{m\,s^{-1}}$ at 200 °C. As expected, the load capacity of the bearing increases with increasing U. The average velocity across the film increases also, resulting in a flow increase through the bearing. The average modified Reynolds number based on the minimum film thickness is about 2·2 and 5·2 for $U = 127{\cdot}0$ and $254{\cdot}0\ \mathrm{m\,s^{-1}}$ respectively. For relatively large U the pressure very close to the bearing exit is much larger than the imposed pressure exactly at the bearing exit. This means that choked flow takes place at the bearing exit. The choked flow conditions (back pressure and maximum flow rate) are predicted by the present method.

Stiffness of an externally pressurized slider bearing

Figures 13–15 demonstrate the stiffness characteristics of the gas bearing between two, in general non-parallel, plates for different geometry configurations based on the analysis presented in this paper. The stagnation pressure and temperature are $p_0 = 3450\ \mathrm{kPa}$ and $T_0 = 200\ ^\circ\mathrm{C}$ respectively. The exit pressure is taken as $p_a = 903{\cdot}2\ \mathrm{kPa}$. Figure 13 shows the influence of the angle between the two planes on the pressure distribution. The film thickness at the entrance and exit is denoted by h_1 and h_2, respectively. It is noted that as h_1 increases, with h_2 kept constant, the load capacity of the bearing increases. Therefore the stiffness of the bearing increases with

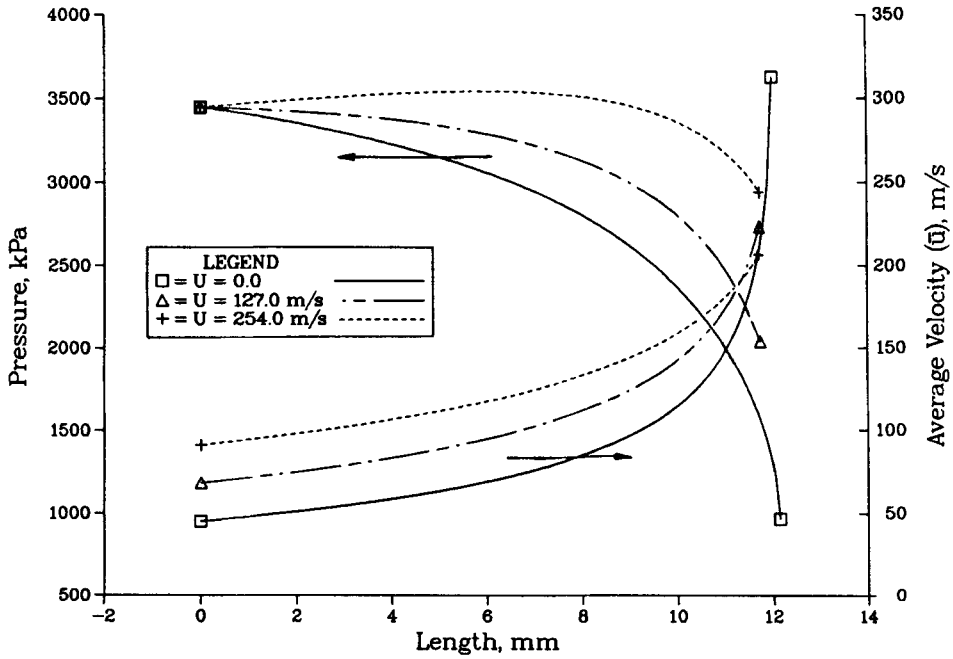

Figure 12. Influence of relative motion between slider planes on pressure and average velocity distributions

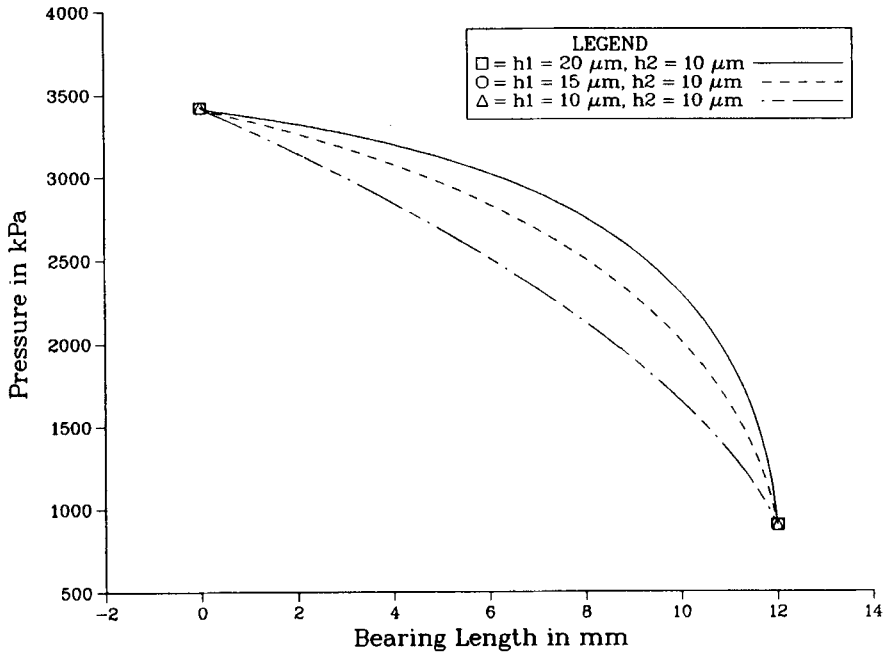

Figure 13. Pressure distribution along bearing for non-choked flow between two non-parallel plates for different angles of inclination between plates

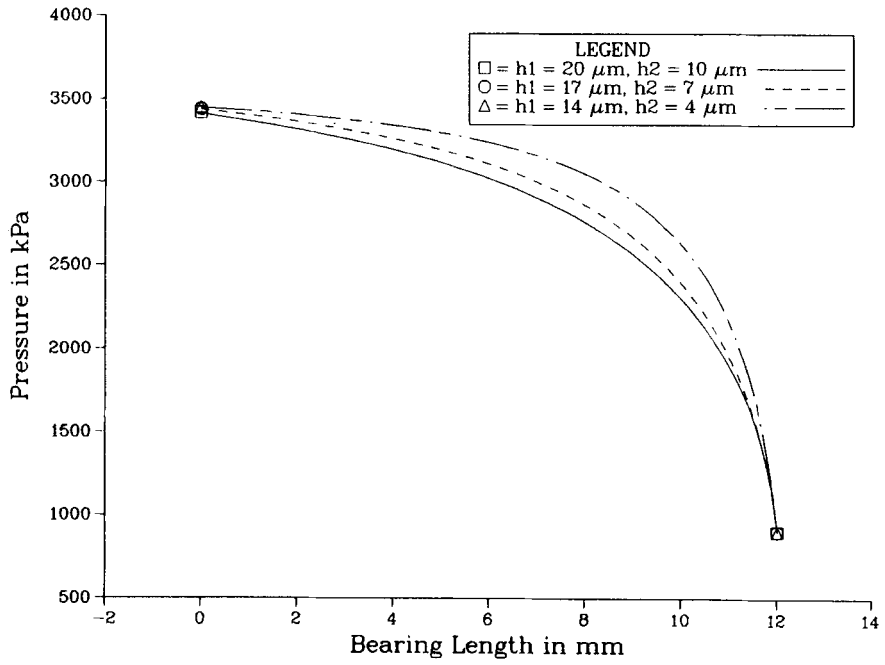

Figure 14. Pressure distribution along bearing for non-choked flow between two non-parallel plates for different minimum film thicknesses

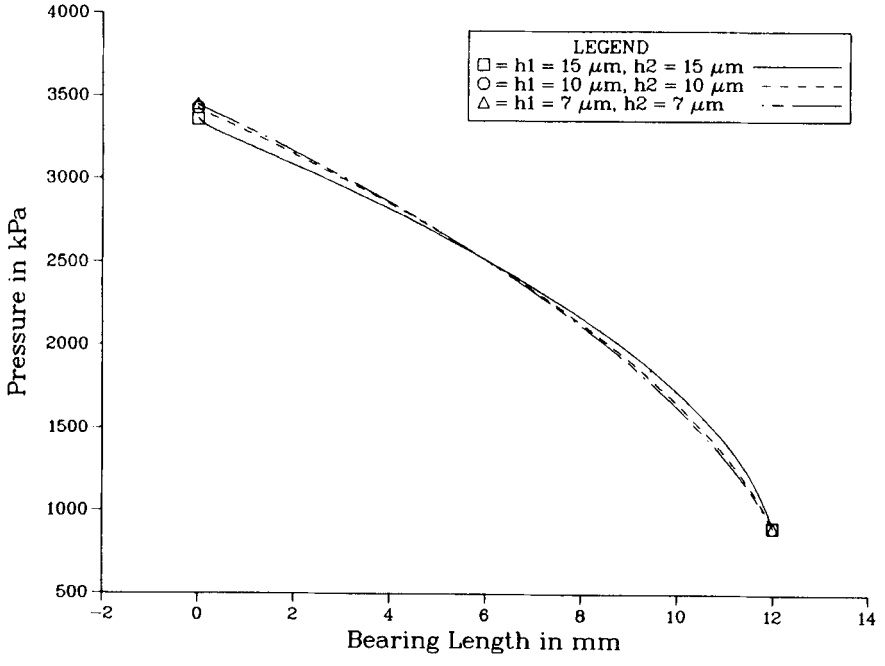

Figure 15. Pressure distribution along bearing for non-choked flow between two parallel plates for different film thicknesses

increasing angle of inclination between the two planes. Figure 14 illustrates the effect of the minimum film thickness between the two planes on the bearing stiffness. Here the angle of inclination between the two planes is kept constant. As the minimum film thickness decreases, the load capacity of the bearing, the consequently the stiffness, increases. However, this is true only when the angle of inclination between the two planes is not zero. In Figure 15 the minimum film thickness changes but the angle of inclination is zero. It is noted that the bearing load capacity remains practically the same or, equivalently, the bearing stiffness is zero. This conclusion can be proven theoretically, when the fluid inertia effect is neglected, from the compressible Reynolds equation (equation (37) in Appendix I). If the angle of inclination between the two planes is zero (constant film thickness), the RHS of equation (37) is zero and therefore the pressure along the bearing is independent of the constant film thickness h.

CONCLUSIONS

1. The results for the present analysis agree very well with available analytical and experimental results.
2. The gas inertia effect is important in high-velocity flow (e.g. choked flow) between two closely spaced plates.
3. The energy effect can be ignored for practical purposes in calculating the flow between two closely spaced plates.
4. The stiffness of an externally pressurized slider bearing (a) increases with increasing angle of inclination between the two plates, (b) increases with decreasing minimum film thickness for non-parallel plates and (c) is practically zero if the two plates are parallel.

APPENDIX I: SOLUTION METHOD FOR COMPRESSIBLE REYNOLDS EQUATION

Under the usual lubrication assumptions for the film separating two closely spaced surfaces, the Navier–Stokes equations and the continuity equation reduce to the following compressible Reynolds equation[3] for the steady state, one-dimensional case using the notation of Figure 16.

$$\frac{\partial}{\partial x}\left(\frac{\rho h^3}{\mu}\frac{\partial p}{\partial x}\right)=6U\frac{\partial(\rho h)}{\partial x}. \tag{37}$$

The density ρ of the working fluid is related to the pressure by the perfect gas relation of equation (3). The boundary conditions associated with equation (37) are as follows for unchoked and choked flow according to the notation of Figure 16.

Unchoked flow

$$p=p_{en} \quad \text{at } x=0, \tag{38}$$

$$p=p_a \quad \text{at } x=L. \tag{39}$$

An isentropic expansion of a perfect gas is assumed from the stagnation properties p_0, T_0 and $u_0=0$ to the gas properties p, T and average velocity $\bar{u}_{en}$ at the entrance. Thus

$$p_{en}=p_0\left(1-\frac{\gamma-1}{2\gamma RT_0}\bar{u}_{en}^2\right)^{\gamma/(\gamma-1)}. \tag{40}$$

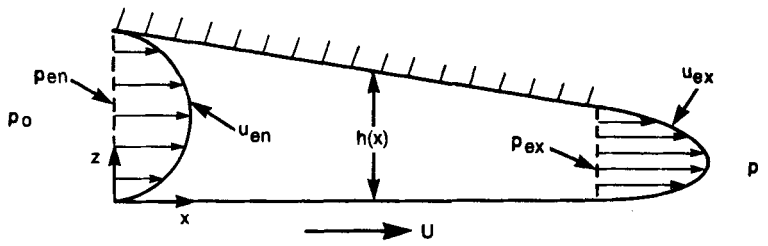

Figure 16. Geometry and notation of gas film for compressible Reynolds equation method

The average velocity at the entrance is given by

$$\bar{u}_{en}=\frac{1}{h(0)}\int_0^{h(0)} u_{en}\,dh. \tag{41}$$

Choked flow

$$p=p_{en} \quad \text{at } x=0. \tag{38}$$

The pressure at the entrance, p_{en}, is given by equation (40). For choked flow the average velocity at the exit, $\bar{u}_{ex}$, is assumed to be equal to the sonic velocity $c=\sqrt{(\gamma RT_0)}$:

$$\bar{u}_{ex}=c. \tag{42}$$

According to lubrication theory, the velocity distribution in the film gap is

$$u(x,z)=\frac{1}{2\mu}\frac{dp}{dx}(z^2-zh)+\left(1-\frac{z}{h}\right)U.$$

The average velocity at the exit is

$$\bar{u}_{ex}=\frac{1}{h(L)}\int_0^{h(L)} u(L,z)dz=-\frac{h(L)^3}{12\mu}\left.\frac{dp}{dx}\right|_{x=L}+\frac{Uh(L)}{2}. \tag{43}$$

Because of equations (42) and (43), the gradient of the pressure at the exit is known and given by

$$\left.\frac{dp}{dx}\right|_{x=L}=\frac{12\mu}{h(L)^3}\left(\frac{Uh(L)}{2}-c\right). \tag{44}$$

Therefore for the case of choked flow the boundary conditions for equation (37) are given by equations (38) and (44).

The solution algorithm for the compressible Reynolds equation and the associated boundary conditions is described in Figure 17. A pressure at the entrance, p_{en}, is assumed and then equation (37) is solved numerically along with the appropriate boundary conditions using the finite element method. The Newton–Raphson method is used to linearize the Reynolds equation while the Galerkin method is employed at each iteration step to solve the resulting linear equations for the correction term.[16] After the solution has been found, the average velocity at the entrance, $\bar{u}_{en}$, is calculated from equation (41) and then used in equation (40) to calculate the corresponding pressure at the entrance, p^*_{en}, due to an isentropic expansion of the gas from the stagnation state to the conditions at the bearing entrance. The algorithm is considered converged if the initially assumed p_{en} is close to p^*_{en} within a tolerance. Otherwise, p_{en} is taken equal to p^*_{en} and the

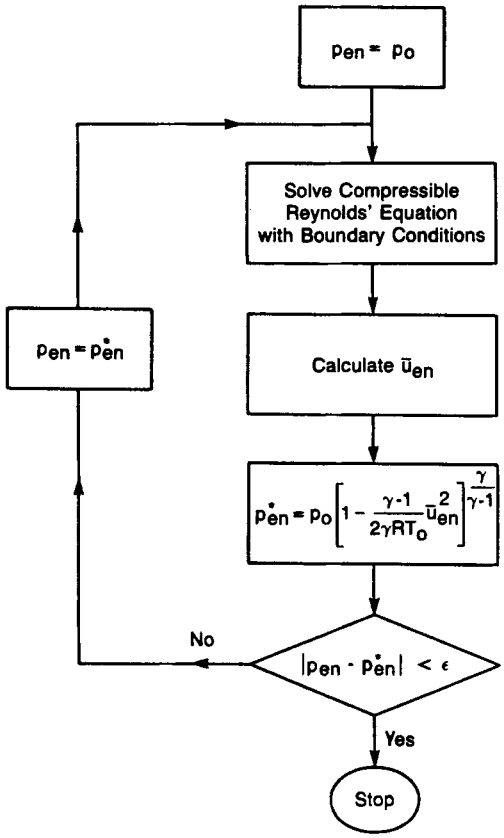

Figure 17. Solution algorithm for compressible Reynolds equation method

boundary value problem is solved again. Three or four iterations are generally needed for the algorithm to converge to the final value of p_{en}. It should be noted that the compressible Reynolds equation method neglects the gas inertia effect (convective terms in the Navier–Stokes equations). This simplification is not realistic for high-velocity flows.

APPENDIX II: NOMENCLATURE

B	bearing breadth
c	sonic velocity
c_p	constant-pressure specific heat of an ideal gas
E	number of quadrilateral finite elements
h	gas film thickness
h	enthalpy
h_1, h_2	entrance and exit film thicknesses
L	bearing length
M	Mach number
N_i^v	finite element velocity shape function of ith node
N_i^p	finite element pressure shape function of ith node

NX, NZ	numbers of nodal points in x- and z-directions
p	pressure
$\bar{p}$	virtual pressure
p_a	bearing back pressure
R	specific gas constant of a gas
Re	Reynolds number
T	temperaure
u, v, w	velocity components in Cartesian co-ordinates (Figure 1)
$\bar{u}$, $\bar{w}$	virtual velocity components in x- and z-directions
$\bar{u}_{en}$, $\bar{u}_{ex}$	average entrance and exit velocities in x-direction
U	velocity of moving plane in x-direction (Figure 1)
W_i	finite element velocity weighting function of ith node
x, y, z	Cartesian co-ordinates (Figure 1)

Greek letters

α_i, β_i	'upwind' coefficients (Figure 5)
γ	ratio of specific heats of an ideal gas
ε	error tolerance for convergence
μ	gas viscosity
ν	dynamic gas viscosity
ρ	gas density
Ω	gas film domain
Ω_e	domain of a gas film finite element

Subscripts

en	entrance
ex	exit
k	iteration number
0	stagnation property

Superscripts

*	non-dimensional value
*	intermediate value

REFERENCES

1. W. A. Gross, *Gas Film Lubrication*, Wiley, New York, 1962.
2. J. T. McCabe, H. G. Elrod, S. Carfagno and R. Colsher, 'Summary of investigations of entrance effects of circular thrust bearings', *Proc. Gas Bearing Symp.*, Southampton, 1969.
3. O. Pinkus and B. Sternlicht, *Theory of Hydrodynamic Lubrication*, McGraw-Hill, New York, 1961.
4. R. A. Burton and Y. C. Hsu, 'The incompressible-turbulent-thin-film short bearing with inertial effects', *ASME J. Lubr. Technol.*, **96**, 158–163 (1974).
5. B. E. Launder and M. Leschziner, 'Flow in finite-width, thrust bearings including inertial effects, I—Laminar flow', *ASME J. Lubr. Technol.*, **100**, 330–338 (1978).
6. V. N. Constantinescu and S. Galetuse, 'On the possibilities of improving the accuracy of the evaluation of inertia forces in laminar and turbulent films', *ASME J. Lubr. Technol.*, **96**, 69–79 (1974).
7. D. C. Kuzma, 'Fluid inertia effects in squeeze films', *Appl. Sci. Res.*, **18**, 15–20 (1967).
8. V. N. Constantinescu, *Gas Lubrication*, Scripta Technica (transl.), American Society of Mechanical Engineers, New York, 1969.
9. A. Z. Szeri, *Tribology: Friction, Lubrication, and Wear*, Hemisphere/McGraw-Hill, New York, 1980.

10. H. Schlichting, *Boundary-Layer Theory*, 7th edn, McGraw-Hill, New York, 1979.
11. J. A. Tichy and W. O. Winer, 'Inertial considerations in parallel circular squeeze film bearings', *ASME J. Lubr. Technol.*, **92,** 588–592 (1970).
12. J. A. Tichy and S. A. Chen, 'Plane slider bearing load due to fluid inertia—experiment and theory', *ASME J. Tribol.*, **107,** 32–38 (1985).
13. J. A. Tichy, 'An approximate analysis of fluid inertia effects in axisymmetric laminar squeeze film flow at arbitrary Reynolds number', *Appl. Sci. Res.*, **37,** 301–312 (1981).
14. H. G. Elrod and T. Y. Chu, 'Inertia and energy effects in the developing gas film between two parallel flat plates', *ASME J. Lubr. Technol.*, **95,** 524–534 (1973).
15. Z. P. Mourelatos, 'Trajectory of a ringless piston within the cylinder of an internal combustion engine with a crosshead design', *Trans. Soc. Automot. Eng.* (1988); also *SAE Paper 880194.*
16. Z. P. Mourelatos, 'Gas lubrication of a ringless piston in an internal combustion engine under dynamic loading', *ASME J. Tribol.*, **110,** 718–726 (1988).
17. M. A. Saad, *Compressible Fluid Flow*, Prentice-Hall, Englewood Cliffs, NJ, pp. 83–131.
18. A. I. Zografos, W. A. Martin and J. E. Sunderland, 'Equations of properties as a function of temperature for seven fluids', *Comput. Methods Appl. Eng.*, **61,** 177–187 (1987).
19. T. J. Chung, *Finite Element Analysis in Fluid Dynamics*, McGraw-Hill, New York, 1978, pp. 267–306.
20. Y. Yamada, K. Ito, Y. Yokouchi, T. Tamano and T. Ohtsubo, 'Finite elements analysis of steady fluid and metal flow', in R. H. Gallagher, J. T. Oden, C. Taylor and O. C. Zienkiewicz (eds), *Finite Elements in Fluids, Vols 1 and 2*, Wiley, New York, 1975, pp. 73–94.
21. P. Hood and C. Taylor, 'Navier Stokes equations using mixed interpolation', in J. T. Oden, O. C. Zienkiewicz, R. H. Gallagher and C. Taylor (eds), *Finite Elements in Flow Problems*, University of Alabama Press, Huntsville, AL, 1974, pp. 121–132.
22. M. D. Olson and S. Y. Tuann, 'Primitive variables versus stream function finite element solutions of the Navier–Stokes equations', in R. H. Gallagher, O. C. Zienkiewicz, J. T. Oden, M. M. Cecchi and C. Taylor (eds), *Finite Elements in Fluids, Vol. 3*, Wiley, New York, 1978, Chap. 4, pp. 73–87.
23. M. Bercovier and O. Pironneau, 'Error estimates for finite element method solution of the Stokes problem in primitive variables', *Numer. Math.*, **33,** 211–224 (1979).
24. K. H. Huebner and E. A. Thornton, *The Finite Element Method for Engineers*, 2nd edn, Wiley, New York, 1982, pp. 164–168.
25. J. C. Heinrich, P. S. Huyakorn, O. C. Zienkiewicz and A. R. Mitchell, 'An upwind finite element scheme for two-dimensional convective transport equation', *Int. j. numer. methods eng.*, **11,** 131–143 (1977).
26. J. C. Heinrich and O. C. Zienkiewicz, 'Quadratic finite element schemes for two-dimensional convective-transport problems', *Int. j. numer. methods eng.*, **11,** 1831–1844 (1977).
27. T. J. Hughes, 'A simple scheme for developing upwind finite elements', *Int. j. numer. methods eng.*, **12,** 1359–1365 (1978).
28. F. M. White, *Viscous Fluid Flow*, McGraw-Hill, New York, 1974.